

Infrared thermography investigation of transitional flow over isolated roughness at high speed

Ye, Qingqing; Schrijer, Ferdinand; Scarano, Fulvio

Publication date

2016

Document Version

Final published version

Published in

51st 3AF International Conference on Applied Aerodynamics

Citation (APA)

Ye, Q., Schrijer, F., & Scarano, F. (2016). Infrared thermography investigation of transitional flow over isolated roughness at high speed. In *51st 3AF International Conference on Applied Aerodynamics: Strasbourg - France* (pp. 1-10). Article FP29-2016-qingqingye

Important note

To cite this publication, please use the final published version (if applicable).
Please check the document version above.

Copyright

Other than for strictly personal use, it is not permitted to download, forward or distribute the text or part of it, without the consent of the author(s) and/or copyright holder(s), unless the work is under an open content license such as Creative Commons.

Takedown policy

Please contact us and provide details if you believe this document breaches copyrights.
We will remove access to the work immediately and investigate your claim.

INFRARED THERMOGRAPHY INVESTIGATION OF TRANSITIONAL FLOW OVER ISOLATED ROUGHNESS AT HIGH SPEED

Qingqing Ye⁽¹⁾, Ferry F. J. Schrijer⁽¹⁾, Fulvio Scarano⁽¹⁾

⁽¹⁾ Faculty of Aerospace Engineering, Delft University of Technology,
Kluyverweg 1, 2629HS Delft, the Netherlands, Email: q.ye-1@tudelft.nl

ABSTRACT

The transitional flow features over and downstream of isolated roughness elements in hypersonic flow are investigated by means of infrared thermography. The local heat flux distribution in the wake of the roughness element reveals the footprint of multiple streamwise counter-rotating vortex pairs. The formation of a turbulent wedge with the spanwise spreading of the wake in the downstream region indicates the early stage of transition and breakdown to turbulence. The onset location of transition is predicted by detecting the origin of the turbulent wedge. Strong dependence of the transition process on the roughness geometry is observed, with significant variations of the lateral spreading rate in the turbulent wedge. Instead, for the present flow conditions negligible variations are associated to changes in Re_h .

1. INTRODUCTION

Boundary layer transition is an important physical process, to be accounted for in the design of hypersonic flight vehicles because of its large impact on the local heat transfer [1]. For a given flight regime, the surface heat flux in the turbulent regime may be up to three times higher than that of a laminar boundary layer leading to higher heat loads to be tolerated by the thermal protection system (TPS). Therefore, in order to further optimize the TPS, an accurate method to predict boundary layer transition is required.

It is well known that the presence of roughness elements with a large enough size will greatly modify the transition mechanism accelerating the process. In general, three dimensional roughness elements produce a system of streamwise counter rotating vortices, which

induce low- and high-speed streaks [2,3], resulting in a spanwise inhomogeneity of the flow. Empirical predictions of roughness induced transition were proposed by Reda [4], who investigated the existing experimental data and proposed a correlation between transition and critical Reynolds number, defined as $Re_h = u_h h / \nu_h$, where u_h and ν_h is the streamwise velocity and kinematic viscosity at the edge of the roughness element. Beyond the critical Reynolds number ($Re_{h, crit}$), the onset of transition moves rapidly upstream towards the roughness element. On the other hand, below the $Re_{h, crit}$, roughness element has little effect on transition. However, since the occurrence of transition depends on a multitude of parameters (roughness geometry, free stream disturbance level, local pressure gradient), significant variations of the $Re_{h, crit}$ have been observed in different flow conditions, rendering a limited range on its application. Furthermore, the physical transition process is not directly taken into account in this correlation.

Experiments in the low-speed flow regime have provided detailed information about the roughness wake flow features and induced transition mechanism, which can help understanding the transition mechanism at high speed. Acarlar and Smith [5] visualized the flow behind a hemisphere roughness element using the dye and hydrogen-bubble-wire flow visualization technique. A periodic shedding of hairpin vortices from the roughness element was observed, which leads to an unstable separated shear layer. They claimed that the shear layer instability caused by the hairpins is closely related to the onset of transition. Ergin and White [6] measured the evolution of the velocity fluctuations in the wake of an array of cylinders using hot-wire anemometry. The velocity fluctuations grow and reach

the turbulent amplitude at supercritical Re_h , indicating a rapid laminar to turbulent transition. The location of maximum velocity fluctuations coincides with the location of the inflection point in the velocity profile, highlighting the importance of shear layer instability and hairpin vortices. In recent tomographic PIV measurements [7,8], the three-dimensional flow organization in the wake of isolated roughness elements (cylinder, square, hemisphere and micro-ramp) was unveiled. The mean flow pattern reveals multiple pairs of streamwise counter-rotating vortices, leading to streaky velocity distribution in the wake. The shedding phenomenon of hairpin-like vortices from the roughness elements was also observed close to the symmetry plane. However, opposing to the observation of previous investigation, the rapid breakdown of these vortices away from the wall indicates that their contribution to the transition process may be negligible.

In addition to experimental investigations, high fidelity computational techniques such as direct numerical simulation (DNS) offer the possibility to characterize the physical mechanism of roughness induced transition with fine details, and help defining better physical models to predict transition. Subbareddy et al. [9] performed DNS computations for a cylinder in hypersonic flow and observed a system of counter-rotating streamwise vortex pairs, which perturb the steady shear flow in the wake of the roughness and later break into hairpin vortices. The increased surface skin friction reveals the signature of the high-speed streaks inducing by the streamwise vortices. The vortex shedding phenomenon at the separated shear layer is again considered to be closely related to the transition mechanism [10]. A similar flow topology was observed by Iyer et al. [3] in the wake of a hemisphere. The sources of unsteadiness are ascribed to the unstable vortex system upstream, the shock-induced unsteadiness and the shear layer instability. To predict the effectiveness of roughness elements in triggering transition, Redford et al. [11] used DNS to study the influence of the Mach number and thermal condition at the wall on isolated roughness induced transition together with the critical roughness height based Reynolds number (Re_h). A correlation was found between the parameter $M_h T_\infty / T_w$ and Re_h to distinguish the steady laminar case from the transitional case. Bernardini et al. [12] proposed a modified roughness Reynolds number $Re_h^* = u_h h / \nu_w$ by using the kinematic viscosity at the wall. In a more recent parametrical study, Bernardini et al. [13] estimated the critical Reynolds number based on the momentum deficit produced by the roughness element. The latter parameter depends strongly on the roughness geometry. However, due to the high computational costs, there is still gap between the maximum Reynolds number reached by DNS and the inflight Reynolds number. To fill the gap, high-

speed wind tunnel experiments on roughness induced transition are necessary, in order not only to understand the physical mechanism, but also to offer database for transition prediction.

Tirtey et al. [14] investigated the flow structure over various roughness elements using a laminar computation and experiments and found that the effectiveness of roughness in causing transition strongly depends on its geometry. High-speed qualitative flow visualization (PLIF) was performed by Danehy et al. [15, 16] over various roughness elements. The dominant flow structures, including the horseshoe and streamwise vortices, were identified. In a three-dimensional experimental investigation, Avallone et al. [17] found two pairs of counter-rotating vortices in the wake of cylinder using tomographic PIV. The vortices induce low- and high-speed regions and high-level velocity fluctuations in the wake.

Further quantitative experiments are necessary to produce a better understanding of the flow topology in the proximity and downstream of the roughness element and to link these flow features to the downstream occurrence of boundary layer transition. In the present study, quantitative infrared thermography was used to study the effect of isolated surface roughness on hypersonic boundary layer transition. The experiments were performed at Mach 7.5 in the Hypersonic Test Facility Delft (HTFD). The local heat flux distribution was obtained to characterize the transitional flow features over isolated roughness element with different geometry (micro-ramps and cylinder). The topological interpretation of the heat transfer maps is aided making use of high fidelity resolution low speed experiments using tomographic particle image velocimetry in order to detect similarities and to gain more insight into the local flow topology. The onset location of transition is estimated based on the observation of the lateral spreading of wake, identifying as the onset of turbulent wedge. Furthermore, the lateral spreading character of turbulent wedge is analyzed.

2. EXPERIMENTAL SETUP AND FLOW CONDITIONS

The experiments were conducted in the Hypersonic Test Facility Delft (HTFD) of Aerodynamics Laboratories at TU Delft [18]. The operation of the wind tunnel follows the Ludwig tube concept and generates a Mach 7.5 freestream having a velocity of 1030m/s. The test section has a diameter of 350mm. The total temperature T_0 is 579K. Two test conditions with different total pressure ($p_0=22$ and 28bar) are considered to investigate the effect of different free-stream Reynolds number, which are 11×10^6 and $14 \times 10^6 \text{m}^{-1}$, respectively. The total duration of the flow in the test section with uniform

conditions is approximately 100ms. The repeatability of the freestream flow conditions is 0.4% [18].

A 5° compression ramp model (200 mm long and 115 mm wide) was installed in the test section by a rear-holding sting (Fig. 1(a)). The leading edge is manufactured with a controlled curvature radius of 50 μ m to avoid leading edge instabilities. The model is made of Makrolon material, which has a low thermal conductivity ($k = 0.2\text{W/mK}$) and relatively high emissivity ($\epsilon = 0.88$), well suited for the application of IR thermography. Four roughness elements (three micro-ramps and one cylinder) are selected to investigate the influence of the roughness size and geometry on the local heat flux distribution. A schematic of the roughness elements is shown in Fig. 1(b). The detailed parameters defining the roughness geometry are summarized in Tab. 1. MR1 is the baseline micro-ramp geometry, while MR2 has a smaller incidence angle (less compression) and MR3 is 50% higher. The roughness elements were positioned at 30mm from the leading edge. The laminar boundary layer properties at the roughness location as obtained from Blasius theory in combination with the Illingworth compressibility correction are summarized in Tab 2. The Mach number at the edge of the boundary layer is 6.5. The origin of the coordinate system that is located at the half chord length of the roughness element. The x and y axis correspond to the streamwise and spanwise direction respectively.

The infrared thermography measurements were carried out with a CEDIP Titanium 530L IR system. The camera detector has an array of MCT sensor material. The sensor has a size of 320 \times 256pixels and a spectral response in the range of 7.7–9.3 μ m. An integration time of 340 μ s was used in the experiment to achieve a satisfactory camera sensitivity. The recording frame rate was 218Hz at full resolution. The resulted spatial resolution is approximately 1.7px/mm. The tunnel is fitted with a Germanium window with the transmissivity of approximately 0.8, providing optical access to the infrared wavelength. The camera is placed in an angle of approximately 30° with respect to the window in order to prevent self-reflections, as shown in Fig. 2. The IR system was calibrated using a reference black body, taking the effect of germanium window and camera inclination angle with respect to the window on transmissivity into consideration. Spurious contributions due to ambient radiation are minimized by shielding the camera with a matt-black sheet.

The convective heat transfer is obtained from the measured transient surface temperature distribution using a one-dimensional semi-infinite wall model, in which the unsteady heat conductive equation (Fourier equation) is solved. The data reduction method is based

on the work by Cook and Feldermann [19] and the present implementation is discussed in detail by Schrijer et al. [20]. The measured surface heat flux q_s is non-dimensionalized using the heat flux values for an undisturbed laminar boundary layer $q_{s, laminar}$, as

$$q^* = q_s / q_{s, laminar} \quad (1)$$

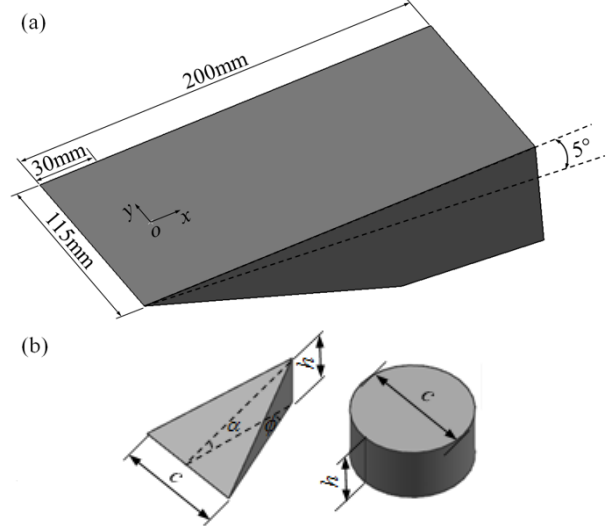


Figure 1. Sketch of the wind tunnel model (a) and roughness elements (b)

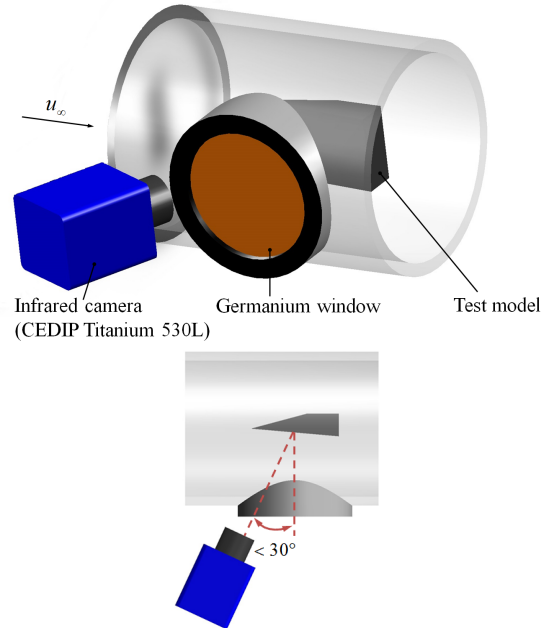


Figure 2. Sketch of the experimental setup, perspective (top) and top view (bottom).

No.	Roughness geometry	c (mm)	h (mm)	α (°)	φ (°)
MR1	Micro-ramp	4	2	24	24
MR2	Micro-ramp	8	2	13	24
MR3	Micro-ramp	6	3	24	24
C1	Cylinder	4	2	-	-

Table 1. Dimensions of roughness element

No.	Low Re	High Re
p_0 (bar)	22	28
Ma_e	6.5	6.5
Re_{unit} (m^{-1})	11×10^6	14×10^6
x_h (mm)	30	30
δ_{99} (mm)	1.2	1.1
θ (mm)	0.15	0.13
Re_θ	1700	1900

Table 2. Laminar boundary layer properties at the roughness location

3. MICRO-RAMP FLOW TOPOLOGY

In low speed flow, where compressibility effects are not considered, the time-averaged transitional wake flow topology over submerged micro-ramp was investigated by tomographic PIV [8]. Two pairs of counter-rotating vortices are identified in the near wake, inducing alternating low- and high-speed regions. For the current conditions, a micro-ramp of the same geometry and size (MR1) is selected first. The time-averaged surface heat flux q^* at Re_h of 2.9×10^4 (referred to as the high Re) is shown in Fig. 3(a). Two high heat load regions at the side of the micro-ramp can be observed, corresponding to the high shear stress at these locations. As proposed by Ye et al. [8], a primary vortex pair originates from the trailing edge of the micro-ramp, inducing a lateral downwash motion and a transport of high momentum flow towards to the wall at the side of the vortices (shown in Fig. 4), causing the increased heat flux levels. In the numerical simulation at hypersonic flow conditions, Tirtay et al. [14] also found these dominant primary vortices in the wake of the micro-ramp. For the sake of clarity, the flow organization behind the micro-ramp is visualized with the aid of a conceptual model, as shown in Fig. 5, in which the vortex structures are shown by colored lines. The low- and high-speed

regions are highlighted with blue and yellow projections on the model surface. Due to the induced upwash motion, the primary vortex pair (TRP) lift up when moving downstream. The high speed regions tend to move close to each other after the lift-up process of the primary vortex pair, so as the high heat flux regions (see Fig. 3(a)). The heat load magnitude undergoes a rapid decrease when moving downstream, which can be attributed to the damping of the streamwise vorticity magnitude. The former high heat load regions from either side of the micro ramp seem to disappear at $x/h = 8$, where a single high heat flux area close to the symmetry axis is observed. This area is associated to a secondary vortex pair with an opposing rotating direction as the primary pair, transporting high-speed flow towards the wall close to the symmetry axis (see Fig. 5). Furthermore, the lateral upwash motion induced by the secondary vortex pair produces two sideward low speed regions. As a result, low heat flux regions, shown as the dark blue streaks, can be observed at the spanwise side of the central high heat flux region in the range $x/h = 8$ to 53.

Further downstream at $x/h = 53$, tertiary higher heat flux regions appear outward of the central peak. The width of the global high heat flux region increases from that location on. This scenario suggests the onset of a turbulent wedge. The process of breakdown to turbulence starts to occur. This observation agrees with the experiment result in the low speed flow [8], where the tertiary pair of streamwise vortices is identified outward of the secondary pair in the downstream region, leading to new pairs of low- and high-speed regions and a spanwise propagation of the overall vortical structures (Fig. 4 and 5). The tertiary vortex pair is acting as the precursor of a turbulent wedge and laminar to turbulent transition.

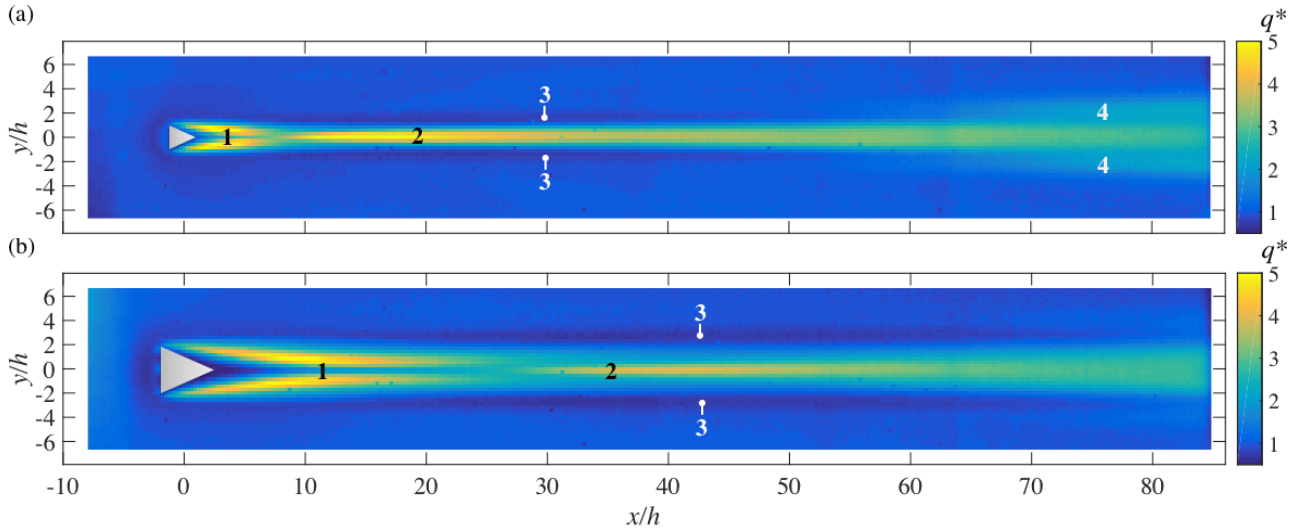


Figure 3. Normalized heat flux distribution q^* over micro-ramp of different incidence angle at $Re_h = 2.9 \times 10^4$, (a) MR1, (b) MR2; 1, 2 and 4 - the primary, secondary and tertiary high heat flux regions; 3-low heat flux regions.

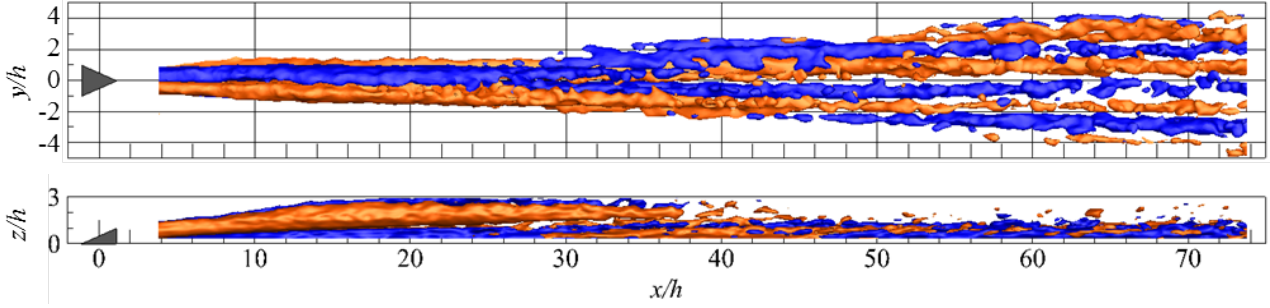


Figure 4. Three-dimensional time-averaged streamwise vorticity field at low speed, $Re_h = 1170$ [8] (blue and red for anticlockwise and clockwise rotation vortices), top (top) and side (bottom) view.

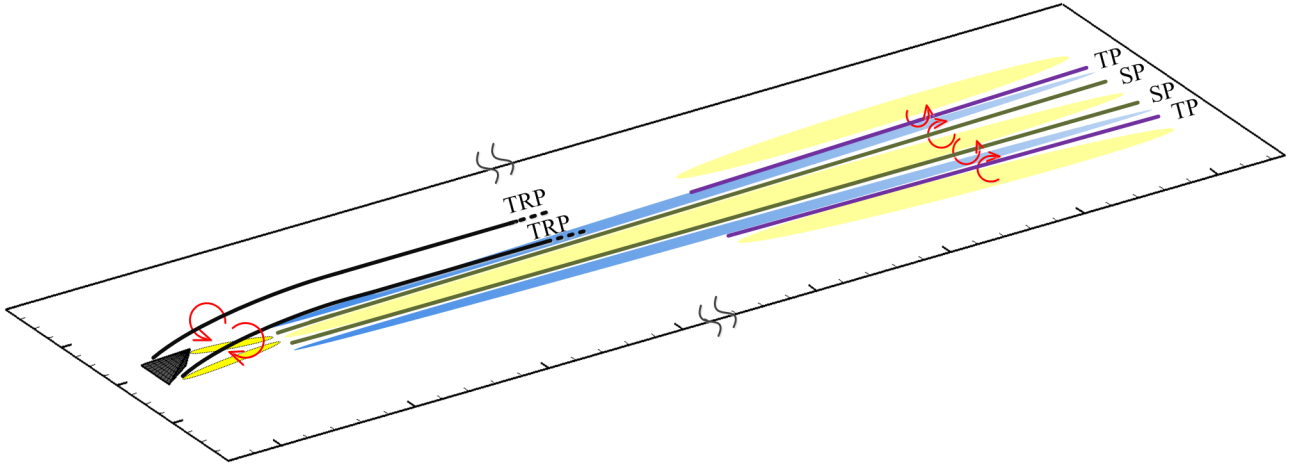


Figure 5. Conceptual sketch of the flow topology in the wake of micro-ramp (MR1) at supercritical Re_h . TRP, SP, and TP: trailing edge, secondary and tertiary vortex pair; blue and yellow projections: low- and high-speed regions

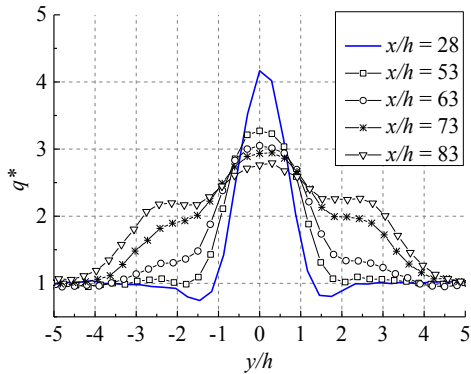


Figure 6. Spanwise heat flux distribution at different streamwise locations in the wake of MR1.

The spanwise surface heat flux distribution at different streamwise locations is provided in Fig. 6. At $x/h = 28$, the central high heat flux region shows a maximum of $4.1q_{s,laminar}$ enclosed by two low heat flux regions at $y/h = \pm 1.5$ that are approximately 30% lower than the undisturbed boundary layer. Moving downstream to the turbulent wedge region $x/h \geq 53$, three maxima of surface heat flux can be observed, corresponding to the secondary and tertiary high heat flux regions. The magnitude of the tertiary maxima increases when

moving downstream. On the other hand, the secondary maximum decreases. The surface heat flux tends to develop into a homogenous distribution inside the wedge. It is assumed here that the flow is approaching an isotropic turbulent regime.

In previous infrared thermography investigation [14, 21], the transition location in the wake of a roughness element is defined as the point where surface heat flux reaches a local minimum followed by a steep increase in the symmetry plane. However, the surface heat flux distribution in the wake of the roughness element is highly three dimensional. The transition prediction based on the selection of a single spanwise location is therefore not always representative for the overall flow field. Moreover, the vortical structures of strong intensity behind the roughness normally lead to overheating areas, such as the primary and secondary high heat flux regions in the wake of the micro-ramp, shown in Fig. 3(a). As a result, one should be very careful when using the rapid surface heat flux increase as a general method to signify laminar to turbulent transition behind roughness element. On the other hand, the breakdown of laminar boundary layer to turbulence behind isolated roughness usually happens by means of the formation and growth of the turbulent wedge, which

is observed to appear far downstream ($45h$) of the starting point of the secondary surface heat flux peak in the wake of micro-ramp (MR1). In this paper, the transition location is defined as the inception of the turbulent wedge at which the width of the wake starts to increase.

4. EFFECT OF MICRO-RAMP INCIDENCE ANGLE

As discussed in section 3, the dominant features in the near wake of micro-ramp are the two pairs of counter-rotating streamwise vortices. The primary vortices are produced by the pressure difference between the front and side/aft of the micro-ramp, pushing the flow to the side. When changing the incidence angle of the micro-ramp, the magnitude of the pressure gradient between the front and the aft/side will also be modified. Therefore, the vorticity magnitude of the primary vortex pair is affected as well, influencing the evolution of the flow field in the wake and the transition process. In the present study, the surface heat flux distribution over two micro-ramps of different incident angles and same height (MR1 and MR2, $\alpha_{MR1} = 24^\circ$, $\alpha_{MR2} = 13^\circ$) are discussed and compared at Re_h of 2.9×10^4 (High Re).

Similar to the heat flux distribution in the wake of MR1, two high heat load regions can also be observed close to the micro-ramp of lower incidence angle (MR2, Fig. 3(b)). The larger micro-ramp span leads to an increase of the spanwise separation of the two primary high heat flux regions. Lower magnitude of the primary heat flux peaks of $4.9q_{s,laminar}$ is obtained with respect to MR1 ($5.8q_{s,laminar}$), indicating a relatively weaker vorticity magnitude of the primary vortex pair. The high heat flux regions remain active in a longer streamwise range until $x/h = 27$. Furthermore, the secondary high and low heat flux regions also appear further downstream compared to the MR1 case. A quantitative comparison of the surface heat flux evolution at the symmetry plane is shown in Fig. 7. The ratio between the theoretical turbulent and laminar heat flux is provided as a reference:

$$q^*_{turb,theo} = q_{turb,theo} / q_{lam,theo} = c_{h,turb} / c_{h,lam} \quad (2)$$

The compressible laminar boundary layer Stanton number is calculated using the reference temperature method by

$$c_{h,lam} = c_f \text{Pr}^{(-2/3)} = \frac{0.664\sqrt{C^*}}{\sqrt{\text{Re}_{x,\infty}}} \text{Pr}^{(-2/3)} \quad (3)$$

where c_f is the skin friction coefficient, Pr is the Prandtl number, C^* is Chapman-Rubesin parameter evaluated using Eckert's correction [22].

For the turbulent boundary layer, the skin friction coefficient is estimated by the van Driest II correlation [23], as

$$\frac{\sin^{-1} A + \sin^{-1} B}{\sqrt{c_f(T_{aw}/T_e - 1)}} = 4.15 \log(\text{Re}_{x,\infty} c_f \frac{\mu_\infty}{\mu_w}) + 1.7 \quad (4)$$

where

$$A = \frac{2a^2 - b}{\sqrt{4a^2 + b^2}}, B = \frac{b}{\sqrt{4a^2 + b^2}} \quad (5)$$

$$a = (r \frac{\gamma - 1}{2} M_\infty^2 \frac{T_\infty}{T_w})^{1/2}, b = \frac{T_{aw}}{T_w} - 1 \quad (6)$$

Then the Stanton number is calculated using Reynolds analogy [23]

$$c_{h,turb} = \frac{1}{2} c_{f,turb} \text{Pr}^{-2/3} \quad (7)$$

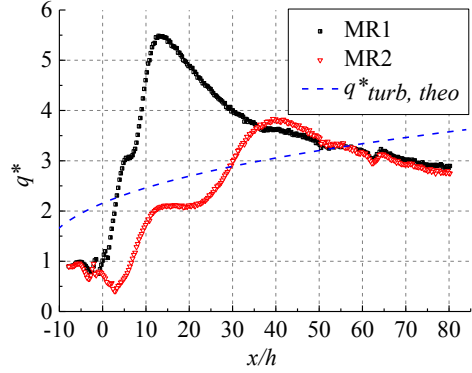


Figure 7. Streamwise evolution of the normalized surface heat flux at the symmetry plane for MR1 and MR2 at $Re_h = 2.9 \times 10^4$.

A steep surface heat flux increase can be observed behind both MR1 and MR2, reaching a maximum of 5.4 and 3.8 times of the undisturbed boundary layer at $x/h = 13$ and 40 respectively and starting to decrease when moving downstream. At $x/h = 50$, the surface heat flux at the symmetry plane behind both micro-ramps reaches the same magnitude and decreases below the turbulent level further downstream. Even at the most downstream region, the wake width of MR2 remains relatively constant. Therefore, turbulent wedge does not occur in the current measurement range. Moreover, although the surface heat flux at the symmetry plane undergoes rapid increase in the upstream region ($x/h = [22, 40]$), the laminar to turbulent transition does not take place behind MR2, further proving that the former phenomenon cannot be used as the indication of transition in the present conditions.

In summary, the micro-ramp having a lower incidence angle produces primary and secondary vortical structures that have lower vorticity magnitude in the wake, thus are less capable to transport momentum towards the wall. Consequently, the surface shear stress is decreased and heat flux values of lower intensity are obtained. The turbulent wedge is not detected in the wake micro-ramp of low incidence angle, indicating the onset of transition is significantly delayed compared with that of larger incidence angle.

5. CYLINDER FLOW TOPOLOGY

For cylindrical roughness element, one dominant flow structure is the system of multiple spanwise vortices in upstream separation region [3, 9, 24]. These vortical structures wrap around the cylinder, leading to streamwise rotating vortices in the wake. Similar to the momentum transport mechanism in the wake of the micro-ramp, these vortices will also transport the low momentum fluid upward, and entrain high momentum fluid down towards the wall, producing low- and high-speed regions. As a result, the associated high surface heat flux regions can be detected on the model surface. The surface heat flux distribution q^* over cylinder (C1) of the same height and span of MR1 are illustrated at two Reynolds numbers $Re_h = 2.3 \times 10^4$ (Low Re) and 2.9×10^4 (High Re) in Fig. 8.

In the upstream separation region, two high heat flux arcs can be detected at $Re_h = 2.3 \times 10^4$. Baker [24]

categorized the system with the number of vortices included as a two-, four-, or six-vortex system. The two high heat flux regions correspond to that produced by the four-vortex system as shown in Baker's conceptual sketch (see Fig. 9(a)). The high heat flux regions are highlighted in red.

Increasing the Re_h to 2.9×10^4 , the number of high heat flux regions increases to 3 arcs, indicating the increased complexity of the vortical system, which correspond to the six-vortex system proposed by Baker [24]. Consequently, the number of vortex pairs in the near wake also increases from two to three with Re_h , detected as 3 pairs of heat flux maxima at $x/h = 15$ in Fig. 10. One can also observe the increase of the width of the wake. Further downstream, the onset location of a turbulent wedge is observed at $x/h = 40$ and 24 respectively. Consequently, when increasing Re_h , a rapid upstream movement of transition process is detected in the wake of cylinder.

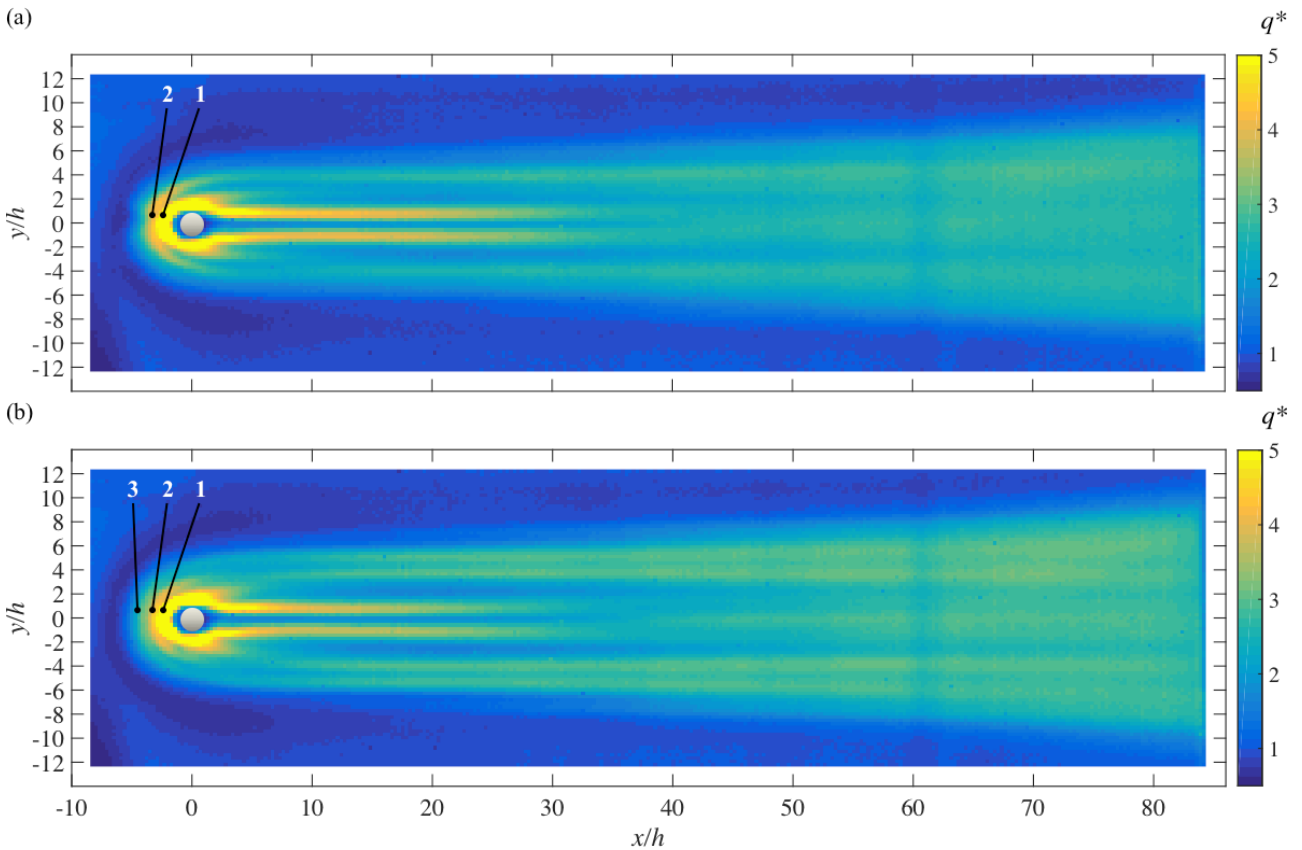


Figure 8. Normalized surface heat flux distribution q^* around cylinder (C1), (a) $Re_h = 2.3 \times 10^4$ (Low Re), (b) $Re_h = 2.9 \times 10^4$ (High Re); 1,2,3: Arc-shape high heat flux regions.

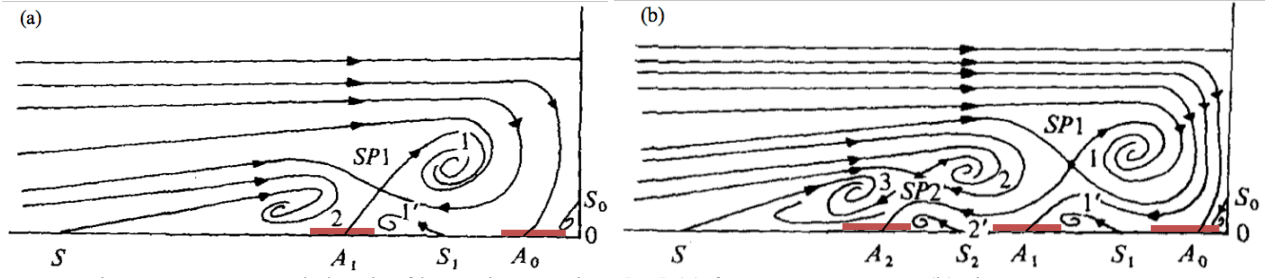


Figure 9. Conceptual sketch of horseshoe vortices [23] (a) four-vortex system, (b) six-vortex system.

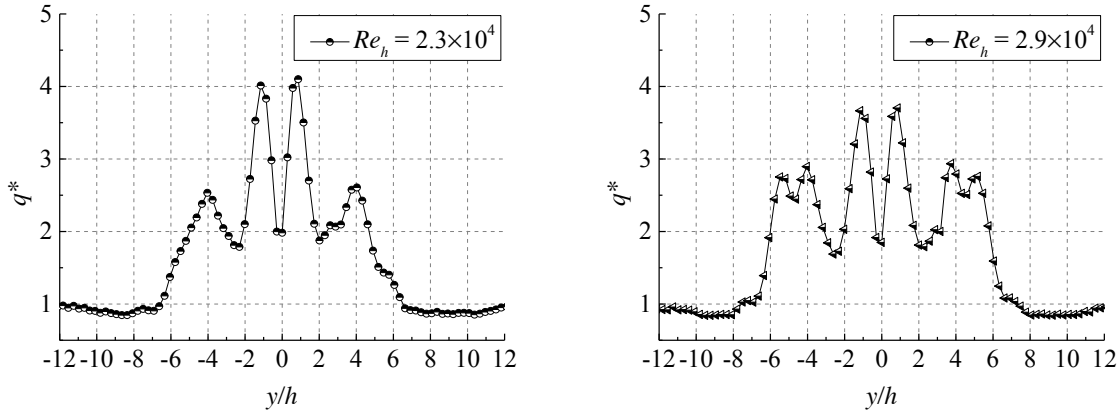


Figure 10. Spanwise distribution of surface heat flux in the wake of cylinder at $x/h = 15$.

6. TURBULENT WEDGE PROPERTY

Behind the isolated roughness element, the onset of transition is characterized by the formation and growth of a turbulent wedge. In the incompressible regime, experimental studies [25, 26] reveal that the turbulent wedge comprises a turbulent core, bounded by an intermittent turbulent region. The fully turbulent core exhibits a smaller lateral growth rate compared with the intermittent region. In the present study, the width of the turbulent wedge (in spanwise direction) till the outer border of the intermittent region (w_c) is measured using the surface heat flux distribution. The outmost border of the turbulent wedge is defined as the intersection point between the constant surface heat flux of the undisturbed boundary layer and the interpolated linear plot depicting the steep increase of heat flux, as shown in Fig. 11. The streamwise evolution of the width of the turbulent wedge is presented in Fig. 12, from which the half spreading angle can be estimated by plotting the wake width in streamwise direction and computing the angle $\beta = \tan^{-1}(w_c/2x)$.

At $Re_h = 2.9 \times 10^4$ (MR1), the spreading angle is found to be $2.2 \pm 0.1^\circ$, which is remarkably smaller than 4.6° observed in incompressible flow. In fact, the lateral spreading of turbulent wedge strongly depends on the Mach number [27]. The compressibility has a stabilizing effect on the growth of disturbances, thus also the lateral spreading rate is decreased [28]. The present result agrees fairly well with the experimental result of Fischer [28], which reported a spreading angle less than 3° at

$Ma = 6.5$.

Besides the confirmed dependence on Mach number, another related parameter, roughness height based Reynolds number Re_h , also influences the spreading angle of the turbulent wedge. In the pioneering investigation on turbulent spots by Schubauer and Klebanoff [25], the spreading angle increases from 8.6° to 10° by tripling the incoming Reynolds number. In a later DNS investigation on a turbulent spot at $Ma = 1.1$ and 5, Jocksch and Kleiser [29] also claim that the spreading angle increases with the Reynolds number. In Fig. 12, the development of lateral spreading of turbulent wedge in the wake of micro-ramp at three Re_h is estimated and compared. The width of the wake shows a stronger dependence on the span of the micro-ramp, while the effect of Re_h on the wake width is negligible. Moreover, opposing to the conclusion from previous investigations on turbulent spots, the spreading angle remains relatively constant of $2.2 \pm 0.1^\circ$ by increasing Re_h from 2.9×10^4 to 4.3×10^4 (1.5 times higher). One should however keep in mind that the present Reynolds number range is rather limited.

In order to further understand the dependence of lateral spreading rate on Re_h , the turbulent wedge behind cylindrical geometry roughness element of with the same aspect ratio (C1) as MR1 is studied, in the wake of which the transition is accelerated compared with a micro-ramp. As a result, the turbulent wedge moves closer to the roughness element, providing a longer

streamwise range for a better development for the wedge in the measurement domain.

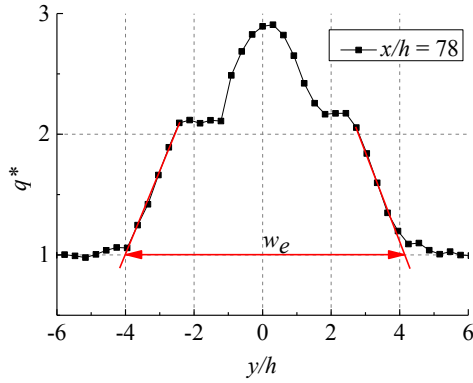


Figure 11. Definition of the border of turbulent wedge.

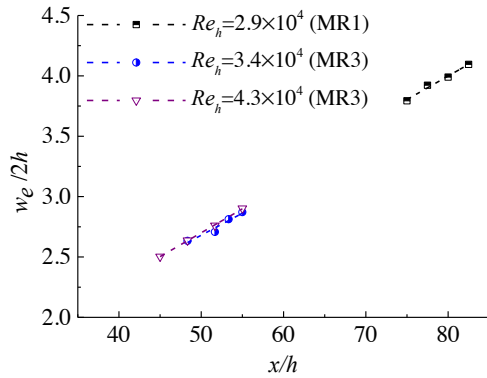


Figure 12. Streamwise evolution of half-width of turbulent wedge behind micro-ramp.

The evolution of wedge width is demonstrated in Fig. 13. The spreading angle of both Re_h have the same value of $3.5 \pm 0.1^\circ$, indicating a comparable lateral growth rate of the turbulent wedge. In addition, the spreading angle increases in the wake of the cylinder compared with the micro-ramp of the same size (MR1 and C1) at the same Re_h , clearly indicating its dependence on the geometry.

From the analysis above, it is found that the spreading angle remains constant behind both micro-ramp and cylinder when increasing Re_h in the present experiment. More experimental data on a significantly larger range of Re_h is needed to provide further information on its effect.

7. CONCLUSION

In the present study, the transitional flow feature over isolated roughness element at Mach 7.5 is analysed using quantitative infrared thermography. The local surface heat flux distribution from upstream to the far wake of four roughness elements of different geometry and size are investigated at three different supercritical roughness-height based Reynolds number Re_h .

In the wake of micro-ramp, primary and secondary high surface heat flux regions are observed in the wake flow, corresponding to the high-speed regions produced by the multiple streamwise counter-rotating vortex pairs. The continuous increase of the wake width indicates the onset of turbulent wedge, which is considered as the starting point of transition process. The incidence angle of micro-ramp has a great impact on the vorticity magnitude of primary vortex pair. The decrease of incidence angle delays the onset of laminar to turbulent transition.

For cylinder, the dominant flow feature is the upstream vortex system, producing several high heat flux regions. The upstream vortices persist to the wake, inducing high heat flux streaks. The onset of transition is significantly accelerated with respect to micro-ramp.

The lateral spreading rate of the turbulent wedge is characterized. Both Mach number and roughness geometry have a strong influence on the spreading angle. On the other hand, the dependence on Re_h is negligible in the current Reynolds range.

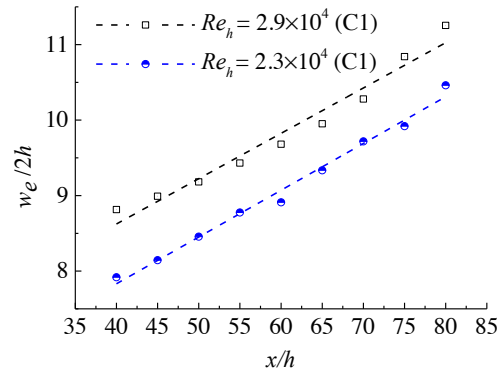


Figure 13. Streamwise evolution of half-width of turbulent wedge behind cylinder.

8. REFERECE

1. Schneider, S. P. (2008). Effects of Roughness on Hypersonic Boundary-Layer Transition. *J. Spacecraft and Rockets* **45**(2), 195-209.
2. Tumin, A. & Reshotko, E. (2005). Receptivity of a Boundary-Layer Flow to a Three-Dimensional Hump at Finite Reynolds Numbers. *Phys. Fluids* **17**, 1-8.
3. Iyer, P. S. and Mahesh, K. (2013). High-speed Boundary-Layer Transition Induced by a Discrete Roughness Element. *J. Fluid Mech.* **729**, 524- 562.
4. Reda, D. C. (2002). Review and Synthesis of Roughness-Dominated Transition Correlations for Reentry Applications. *J. Spacecraft Rockets* **39**(2), 161-167.

5. Acarlar, M. S. & Smith C. R. (1987). A study of hairpin vortices in a laminar boundary layer. part 1. Hairpin vortices generated by a hemispherical protuberance. *J. Fluid Mech.* **175**, 1–41.
6. Ergin F. G. & White E. B. (2006). Unsteady and transitional flows behind roughness elements. *AIAA J.* **44**(11): 2504-2514.
7. Ye, Q., Schrijer, F. F. J. & Scarano, F. (2015). Geometry effect of isolated roughness on boundary layer transition investigated by tomographic PIV. 9th International Symposium on Turbulence and Shear Flow Phenomena. Melbourne, Australia.
8. Ye, Q., Schrijer, F. F. J. & Scarano, F. (2016). Boundary layer transition mechanisms behind a micro-ramp. *J. Fluid Mech.* **793**, 32-161.
9. Subbareddy, P. K., Bartkowicz, M. D. & Candler, G. V. (2014) Direct Numerical Simulation of High-Speed Transition due to an Isolated Roughness Element,” *J. Fluid Mech.* **748**, 848-878.
10. De Tullio, N., Paredes , P., Sandham, N. D. & Theofilis, V. (2013). Laminar–Turbulent Transition Induced by a Discrete Roughness Element in a Supersonic Boundary Layer. *J. Fluid Mech.* **735**, 613–646.
11. Redford, J. A., Sandham, N. D. & Roberts, G. T. (2010). Compressibility Effects on Boundary-Layer Transition Induced by an Isolated Roughness Element. *AIAA J.* **48**(12), 2818-2830.
12. Bernardini, M., Pirozzoli, S. & Orlandi, P. (2012). Compressibility Effects on Roughness-Induced Boundary Layer Transition. *Int. J. Heat Fluid Fl.* **35**, 45–51.
13. Bernardini, M., Pirozzoli, S., Orlandi, P. & Lele, S. K. (2014). Parameterization of Boundary-Layer Transition Induced by Isolated Roughness Elements. *AIAA J.* **52**(10), 2261-2269.
14. Tirtey, S. C., Chazot, O. & Walpot, L. (2011). Characterization of Hypersonic Roughness-Induced Boundary-Layer Transition. *Exp. Fluids* **50**, 407–418
15. Danehy, P.M., Bathel, B.F., Ivey, C.B., Inman, J.A. & Jones, S.B. (2009). NO PLIP Study of Hypersonic Transition over a Discrete Hemispherical Roughness Element. AIAA paper 2009-394
16. Danehy, P.M., Ivey, C.B., Inman, J.A., Bathel, B.F., Jones, S.B., McCrea, A.C., Jiang, N., Webster, M., Lempert, W., Miller, J., & Meyer, T. (2010). High-Speed PLIF Imaging of Hypersonic Transition over Discrete Cylindrical Roughness. AIAA paper 2010-703.
17. Avallone, F., Ye, Q., Schrijer, F. F. J., Scarano, F. & Cardone, G. (2014) Tomographic PIV Investigation of Roughness-Induced Transition in a Hypersonic Boundary Layer. *Exp. Fluids* **55**(1852), 1-12.
18. Schrijer, F. F. J. & Bannink, W. J. (2010). Description and Flow Assessment of the Delft Hypersonic Ludwieg Tube. *J. Spacecraft Rockets* **47**(1), 125-133.
19. Cook, W. J. & Felderman, E. J. (1966). Reduction of data from thin-film heat-transfer gages: A concise numerical technique. *AIAA J.* **4**(3): 561-562.
20. Schrijer, F. F. J., Scarano, F., & van Oudheusden, B. W. (2003). Experiments on hypersonic boundary layer separation and reattachment on a blunted cone-flare using quantitative infrared thermography, AIAA 2003–6967.
21. Avallone, F., Schrijer, F. F. J., & Cardone, G. (2016). Infrared thermography of transition due to isolated roughness elements in hypersonic flows. *Phys. Fluids* **28**, 1-19.
22. Eckert, E. R. G. (1956). Engineering relations for heat transfer and friction in high-velocity laminar and turbulent boundary-layer flow over surface with constant pressure and temperature. *Trans. Am. Soc. Mech. Eng.* **78**, 1273–1283.
23. White, F. M. (1991). *Viscous fluid flow, second edition*. McGraw-Hill Inc, USA, pp550-551.
24. Baker, C. J. (1979). The laminar horseshoe vortex. *J. Fluid Mech.* **95**(2), 347 – 367.
25. Schubauer, G.B. & Klebanoff, P. S. (1954). Contributions on the mechanics of boundary-layer transition. NACA TN-3178, 853-863.
26. Zhong, S., Chong, T. P., & Hodson, H. P. (2003). A comparison of spreading angles of turbulent wedges in velocity and thermal boundary layers. *J. Fluids Eng.* **125**, 267-274.
27. Krishnan, L. & Sandham, N. D. (2006). Effect of Mach number on the structure of turbulent spots. *J. Fluid Mech.* **566**, 225–234.
28. Fischer, M. C. (1972). Spreading of a turbulent disturbance. *AIAA J.* **10**(7), 957–959.
29. Jocksch, A. & Kleiser, L. (2008). Growth of turbulent spots in high-speed boundary layers on a flat plate. *Int. J. Heat Fluid Fl.* **29**, 1543-1557.